J. Non-Newtonian Fluid Mech. 159 (2009) 64–71

Contents lists available at ScienceDirect

Journal of Non-Newtonian Fluid Mechanics

journal homepage: www.elsevier.com/locate/jnnfm

Beads-on-string formation during filament pinch-off: Dynamics with the PTT model for non-affine motion

Pradeep P. Bhat[a,b], Matteo Pasquali[b,**], Osman A. Basaran[a,*]

[a] School of Chemical Engineering, Purdue University, West Lafayette, IN 47907, USA
[b] Department of Chemical and Biomolecular Engineering, and Computer and Information Technology Institute, Rice University, Houston, TX 77005, USA

ARTICLE INFO

Article history:
Received 28 February 2008
Received in revised form
13 November 2008
Accepted 29 January 2009

Keywords:
Filament stretching
Drop breakup
Viscoelastic flow
Beads-on-string
PTT
Gordon–Schowalter

ABSTRACT

Fundamental understanding of the formation and pinch-off of viscoelastic filaments is important in applications involving production of drops (e.g., ink-jet printing, micro-arraying, and atomization). In addition to delaying pinch-off, in some cases, viscoelasticity is known to cause the so-called beads-on-string structure, i.e., a number of small droplets interconnected by thin filaments. In a recent publication [H. Matallah, M.J. Banaai, K.S. Sujatha, M.F. Webster, J. Non-Newtonian Fluid Mech. 134 (2006) 77–104], it was shown that the simulation of an elongating filament modeled by the Phan-Thien/Tanner (PTT) equation with the Gordon–Schowalter (GS) convected derivative, which allows non-affine motion of polymer molecules in the continuum, results in the formation of the beads-on-string structure. On the other hand, such bead formation is not reported in calculations with other viscoelastic models that are also strain-hardening like the PTT model but do not have the GS convected derivative (see, e.g., [M. Yao, S.H. Spiegelberg, G.H. McKinley, J. Non-Newtonian Fluid Mech. 89 (2000) 1–43]). This starkly different behavior of the PTT equation with the GS convected derivative is investigated here. During the elongation of the filament, regions of shear form inside the filament due to its initially curved surface. Because of the presence of the GS convected derivative in the PTT equation – which is known to cause unphysical oscillations in stress in simple step shear flow – the shear stress within the PTT filament exhibits temporal oscillations. The onset of these oscillations coincides with the symmetrical migration of the location of the single maximum in the axial component of the rate-of-strain tensor from the center of the filament to two other locations, one in each half of the filament. This is followed by a similar movement of the location of the maximum in the axial elastic stress inside the filament. These two events eventually lead to the formation of a bead-like structure. The occurrence of the bead is also shown to depend on the extent of the polymer contribution to the total viscosity compared to that of the solvent.

1. Introduction

Formation and breakup of liquid filaments into drops is important in widely practiced applications such as ink-jet printing [1] and atomization [2], and in more recent applications such as micro-arraying of DNA [3] and printing of biological cells [4]. All these applications involve the thinning and the eventual rupture of liquid filaments. Because of the presence of macromolecules such as polymers (as additives in, e.g., inks, or as final products, e.g., DNA in DNA micro-arraying), liquids used in these applications are viscoelastic in nature. Thus, incorporation of viscoelasticity is important in the analysis and better design of these processes. The presence of polymers, even in small amounts, results in the delayed breakup of filaments [5], and in some cases, the breakup of filaments is preceded by the formation of what is called the beads-on-string structure, i.e., a structure that has a number of droplets interconnected by small filaments [6]. These features are not seen in the breakup of Newtonian filaments [7].

Thinning of filaments is also exploited in extensional rheometry. For example, in the filament stretching extensional rheometer (FISER), a vertical column of liquid held between two plates or a liquid bridge is stretched by separating the plates [8,9]. The mid-plane diameter of the thinning filament is recorded, and this data is then used to calculate the elongational viscosity of the liquid. Because of the similarity between the filament breakup in such experiments to that in the formation of drops, the stretching bridge is also used as a model system to study the dynamics of pinch-off [10–13]. A slight modification of this system, which consists of deforming bubbles inside filaments, is used to model the behavior of tacky materials that are subjected to stretching [14,15].

* Corresponding author. Tel.: +1 765 494 4061; fax: +1 765 494 0805.
** Corresponding author. Tel.: +1 713 348 5830; fax: +1 713 348 5478.
E-mail addresses: pbhat@purdue.edu (P.P. Bhat), mp@rice.edu (M. Pasquali), obasaran@purdue.edu (O.A. Basaran).

0377-0257/$ – see front matter © 2008 Elsevier B.V. All rights reserved.
doi:10.1016/j.jnnfm.2009.01.004

It has always been of interest to see if the occurrence of beads-on-string feature seen in filament thinning experiments [16] can be captured using numerical calculations. However, numerical analyses of elongating filaments reported in [11,17–19] do not show formation of such beads. In these papers, strain-hardening models such as the Giesekus [20], the FENE-P [21], the FENE-CR [22], and the Phan-Thien/Tanner (PTT) [23] model without the Gordon–Schowalter (GS) convected derivative [24] have been used. Exceptions to this observation were published recently by Matallah et al. [19,25]. These authors have shown the occurrence of bead-like structures in simulations with the PTT equation that has the GS derivative. This characteristically different behavior of the PTT model is closely examined in this paper. First, a brief description of the GS convected derivative and its criticism are given.

Some viscoelastic constitutive models with non-affine motion of polymer molecules, such as the Johnson–Segalman equation [26] and the PTT equation, use the GS convected derivative of the elastic stress tensor $\boldsymbol{\sigma}$, which is

$$\mathring{\boldsymbol{\sigma}} = \frac{\partial \boldsymbol{\sigma}}{\partial t} + \mathbf{v}\cdot\nabla\boldsymbol{\sigma} - (\nabla\mathbf{v})^T\cdot\boldsymbol{\sigma} - \boldsymbol{\sigma}\cdot\nabla\mathbf{v} + \xi(\mathbf{D}\cdot\boldsymbol{\sigma} + \boldsymbol{\sigma}\cdot\mathbf{D}) \quad (1)$$

where $\mathbf{v}$ is velocity, $\nabla \equiv \partial/\partial\mathbf{x}$ is the usual spatial gradient, $\partial/\partial t$ is the partial time derivative, $\mathbf{D} = [\nabla\mathbf{v} + (\nabla\mathbf{v})^T]/2$ is the rate-of-strain tensor, and ξ is an empirical coefficient that is associated with the "slippage" of polymer strands in the continuum. In the absence of any slippage, $\xi = 0$ and the motion of the polymer molecules is said to be affine. The motion is non-affine otherwise (i.e., for $\xi \neq 0$). When $\xi = 0$, the above equation reduces to the upper-convected derivative of $\boldsymbol{\sigma}$. Constitutive equations that have the GS derivative are known to (1) disobey the *Lodge-Meissner relationship* [27] and (2) show unphysical oscillations in step and start-up steady shear flows [28]. With this background, it is interesting to note that Matallah et al. [19] report formation of bead-like structures in simulations of stretching PTT filaments for non-zero values of ξ. Investigation of this striking feature of the PTT model is the main goal of this paper.

The present paper is organized in the following manner. Section 2 presents the governing equations and the numerical method used. A detailed discussion of the results is taken up in Section 3, and key observations of the present analysis are summarized in Section 4.

2. Equations and numerical analysis

2.1. Transport equations

In an incompressible and isothermal system, in the absence of body forces, the dynamics of filament pinch-off is governed by the continuity equation $\nabla\cdot\mathbf{v} = 0$ and the momentum balance equation $\rho(\partial\mathbf{v}/\partial t) + \rho\mathbf{v}\cdot\nabla\mathbf{v} - \nabla\cdot\mathbf{T} = \mathbf{0}$, where ρ is the density of the liquid, and $\mathbf{T}$ is the Cauchy stress tensor. The stress tensor $\mathbf{T}$ is split into an isotropic part, a viscous part, and an elastic part as $\mathbf{T} = -p\mathbf{I} + \boldsymbol{\tau} + \boldsymbol{\sigma}$, where p is the pressure, $\mathbf{I}$ is the identity tensor, and $\boldsymbol{\tau}$ is the viscous stress tensor. The viscous stress tensor $\boldsymbol{\tau}$ is defined by the Newton's law of viscosity $\boldsymbol{\tau} = 2\eta_s\mathbf{D}$, where η_s is the solvent viscosity.

The polymer contribution to the Cauchy stress in a PTT fluid is modeled by the conformation tensor based constitutive equation [29], where the microstructural features of polymer solutions is represented by a single variable, the conformation tensor (for more details, see [30–33]). The transport equation for the dimensionless conformation tensor $\mathbf{M}$ in an isothermal flow neglecting diffusion is

$$\frac{\partial\mathbf{M}}{\partial t} = -\mathbf{v}\cdot\nabla\mathbf{M} + (1-\xi)(\mathbf{M}\cdot\mathbf{D} + \mathbf{D}\cdot\mathbf{M}) + \mathbf{M}\cdot\mathbf{W} + \mathbf{W}^T\cdot\mathbf{M} - \frac{1}{\lambda}[1 + \epsilon(\mathrm{tr}\,\mathbf{M} - 3)](\mathbf{M} - \mathbf{I}) \quad (2)$$

where $\mathbf{W} = [\nabla\mathbf{v} - (\nabla\mathbf{v})^T]/2$ is the vorticity tensor, λ is the characteristic relaxation time of the polymer, $\mathrm{tr}\,\mathbf{M}$ is the trace of $\mathbf{M}$, and ξ and ϵ are the parameters of the PTT model. Here, the function in the PTT model that depends on the trace of the elastic stress (function Y in Eq. 13 of Phan-Thien [34]) is linear in that quantity (same as in [19]).

The elastic stress tensor $\boldsymbol{\sigma}$ is obtained from the conformation tensor $\mathbf{M}$ as [35] $\boldsymbol{\sigma} = 2\zeta(\mathbf{M} - \mathbf{I})\cdot(\partial a/\partial\mathbf{M})$, where $a(\mathbf{M})$ is the Helmholtz free energy per unit volume and ζ is a function that represents the resistance of the polymer molecules to rotation. For the PTT model, $\zeta = (1-\xi)$ and $a(\mathbf{M}) = (G/2\zeta)\,\mathrm{tr}\,\mathbf{M}$, where $G = \eta_p/\lambda$ is the elastic modulus and η_p is the polymer contribution to the total viscosity η_0 $(= \eta_s + \eta_p)$.

As the transport equations are solved simultaneously with the equations governing the mesh used in the numerical analysis and the equations that arise due to the type of discretization chosen (see below), the governing boundary and initial conditions are given in Section 2.3.

2.2. Numerical method

The numerical method used here is the same as in Bhat et al. [11]. Only a brief account of the method is presented here; for more details, see [11].

Elliptic mapping method of de Santos [36] is used to determine the location of the mesh points. It involves the solution of the elliptic differential equation $\nabla\cdot(\mathcal{D}\cdot\nabla\boldsymbol{\varsigma}) = \mathbf{0}$ where $\boldsymbol{\varsigma}$ is the mapping of the position in the computational domain to that in the physical domain and the dyadic $\mathcal{D}$ controls the spacing of the coordinate lines. The position in the physical domain, $\mathbf{x}$, is obtained from the inverse mapping function $\mathbf{x} = \mathbf{x}(\boldsymbol{\varsigma})$.

The DEVSS-TG/SUPG finite element method [29,37,38] is used to discretize the mapping and transport equations. It involves interpolation of the velocity gradient and the new variable so obtained, the interpolated velocity gradient, is then introduced into the transport equations by modifying them accordingly. (See [29] for more details.)

Finally, a fully implicit predictor-corrector scheme with adaptive stepping is used for time integration [39]. The resulting algebraic equations are solved using Newton's method with an analytical Jacobian matrix. The linear algebra solver is based on the frontal algorithm of Duff et al. [40].

2.3. Problem setup

Fig. 1 shows a schematic of an axisymmetric liquid bridge being stretched between moving top and bottom plates with equal radii

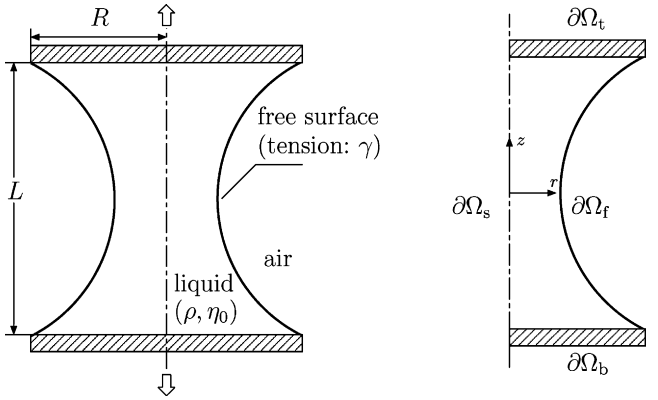

Fig. 1. Left: a schematic of a liquid bridge between moving top and bottom plates. L is the length of the bridge, R is the radius of the plates, ρ is the density of the liquid, η_0 is its viscosity, and γ is the surface tension. Right: computational flow domain and its boundaries.

R. The plates are separated exponentially with a constant stretch rate $\dot{\varepsilon}$. The resulting Hencky strain is $\varepsilon = \dot{\varepsilon}t$.

The boundary conditions on the transport equations and the mesh equation are as follows.

- Along the top and the bottom plate, $\partial\Omega_t$ and $\partial\Omega_b$: No slip and no penetration, i.e., $v_z = v_z(t)$, and $v_r = 0$, where v_z is the axial (z) and v_r is the radial (r) component of the velocity in a cylindrical coordinate system (r, z) with its origin located along the axis of symmetry half way between the two plates. $v_z(t) = \pm\dot{\varepsilon}(L_0/2)e^{\dot{\varepsilon}t}$ (positive sign at the top plate; negative, at the bottom plate), where L_0 is the initial length of the filament. The axial positions of the mesh points are given the same translation as the plates and their radial positions are held fixed. This also ensures that the contact lines at the edges of the two plates are held fixed.
- Along the axis of symmetry, $\partial\Omega_s$: No penetration, i.e., $\mathbf{n}\cdot\mathbf{v} = 0$, and vanishing shear stress, i.e., $\mathbf{tn} : \mathbf{T} = 0$, where $\mathbf{n}$ is the unit normal, and $\mathbf{t}$ is the unit tangent to the boundary. The radial positions of the mesh points are held fixed ($r = 0$) and the axial positions are adjusted such that the coordinate lines are orthogonal to one another.
- Along the free surface, $\partial\Omega_f$: The force balance across the interface is applied through the traction boundary condition [41,42], $\mathbf{n}\cdot\mathbf{T} = -p_a\mathbf{n} + (2H\gamma)\mathbf{n}$, where p_a is the ambient pressure (i.e., in the gas phase), γ is the surface tension of the liquid–gas interface, and H is the mean curvature. The component of the mesh equation that aligns with the normal to the free surface is subjected to the kinematic boundary condition $\mathbf{n}\cdot(\mathbf{v} - \mathbf{v}_s) = 0$ [42], where $\mathbf{v}_s$ is the velocity of the nodes at the free surface; the component that aligns with the tangent to the free surface is subjected to a boundary condition that is given by a function which makes the spacing of the nodes uniform.

The initial condition for computations is that of a cylindrical liquid column at rest with no extra stresses, i.e., $\mathbf{v} = \mathbf{0}$, $p = 0$, and $\boldsymbol{\sigma} = \mathbf{0}$.

The dynamics of stretching viscoelastic filaments is governed by the following dimensionless numbers: Reynolds number, $Re = \rho\dot{\varepsilon}R^2/\eta_0$; capillary number, $Ca = \eta_0\dot{\varepsilon}R/\gamma$; viscosity ratio, $\beta = \eta_s/\eta_0$; Deborah number, $De = \lambda\dot{\varepsilon}$; and the initial aspect ratio of the filament, $\Lambda_0 = L_0/R$. Re represents the ratio of inertial to viscous forces, Ca represents the ratio of viscous to surface tension forces, β gives the solvent contribution to the total viscosity, De represents the ratio of polymer relaxation time to the characteristic flow time, and Λ_0 represents the initial slenderness of the filament (the higher the Λ_0, the slender the filament). In addition to these dimensionless numbers, the PTT model parameters, ξ and ϵ, also affect the dynamics.

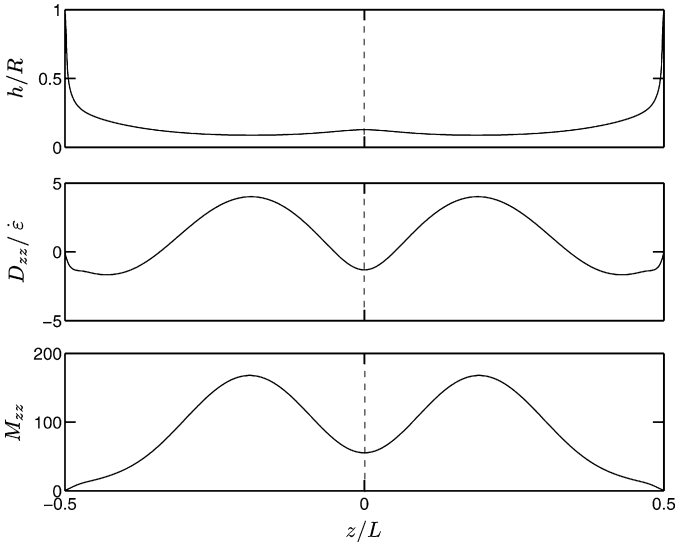

Fig. 3. Variation of the interface height, h/R, along the length of the filament, and the variation of the axial component of the rate-of-strain tensor D_{zz} normalized with $\dot{\varepsilon}$ and that of the conformation tensor M_{zz} along the axis of symmetry ($r = 0$) at Hencky strain $\varepsilon = 3.6$. The viscoelastic model is the PTT model and the parameters are $\Lambda_0 = 0.54$, $Re = 0$, $Ca = 18.26$, $De = 1.89$, $\beta = 0.262$, $\epsilon = 0.035$, and $\xi = 0.13$.

3. Dynamics of PTT filaments

First, we report results of simulations for a PTT filament with parameters whose values are the same as in [19] and at which these authors observed formation of a bead-like structure on the filament. The parameters are $\Lambda_0 = 0.54$, $Re = 0$, $Ca = 18.26$, $De = 1.89$,

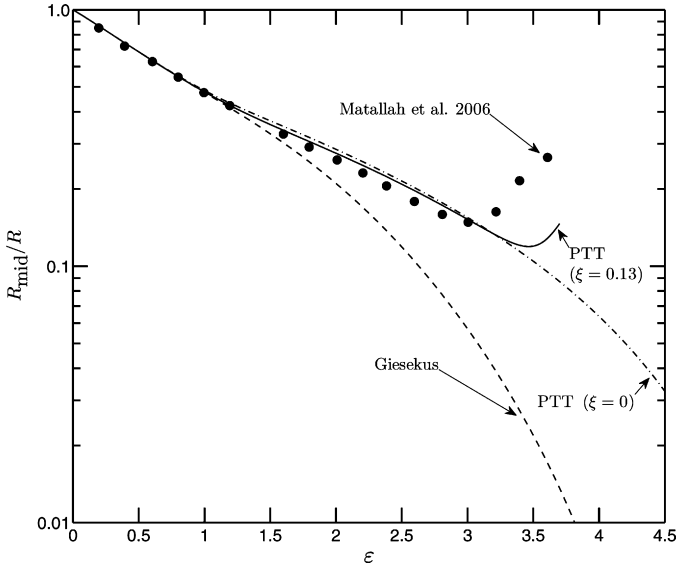

Fig. 2. Variation of the mid-filament radius R_{mid}/R with Hencky strain ε for different models. Here, $\Lambda_0 = 0.54$, $Re = 0$, $Ca = 18.26$, $De = 1.89$, $\beta = 0.262$, $\epsilon = 0.035$ (PTT), and $\alpha = 0.32$ (Giesekus).

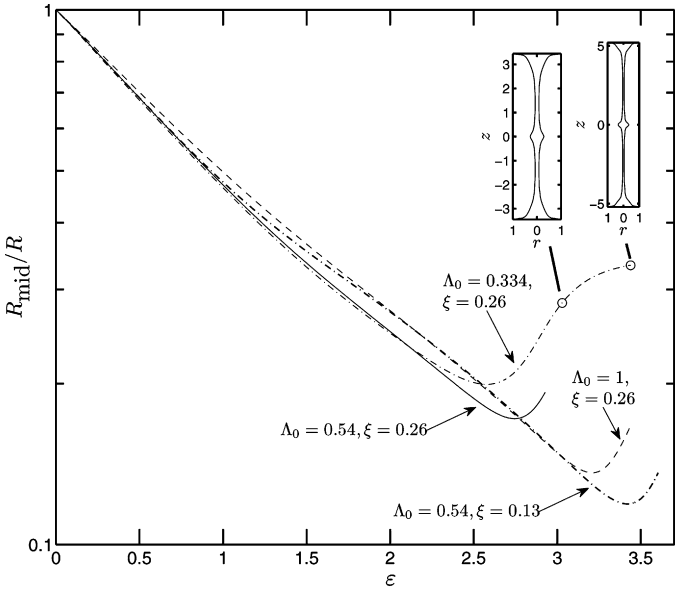

Fig. 4. Variation of the mid-filament radius R_{mid}/R with Hencky strain ε at different Λ_0. Here, $Re = 0$, $Ca = 9.86$, $De = 1.89$, $\beta = 0.262$, and $\epsilon = 0.035$. The insets show filament profiles at different strains.

$\beta = 0.262$, $\epsilon = 0.035$, and $\xi = 0.13$. Fig. 2 shows the comparison of the mid-filament radius, R_{mid}/R, obtained from our calculations with those from [19]. Our results are mesh and time-step converged. (See Bhat et al. [11] for a detailed study of the mesh and time-step convergence characteristics of the numerical method used here.) The data from [19] were obtained by tracing the plot of R_{mid}/R vs. ε in Fig. 4 of [19] using the `datathief` (NIKHEF-K) tracing program. It can be inferred from the two results that a bead-like structure has formed at the center of the filament at higher strains – evident from the fact that R_{mid} increases with ε at these values of the strain. Although bead formation is evinced in both calculations, the results do not match. We see the onset of bead formation at a strain higher than what is reported in [19], and there are differences in the R_{mid} values from the two calculations at intermediate strains as well. These differences between the results are explained later in this section. It is important to note that bead formation occurs only for non-zero values of ξ, and it is absent when $\xi = 0$. Fig. 2 also shows R_{mid} results for the PTT model with $\xi = 0$ and the Giesekus model – another strain-hardening model like the PTT model but without the GS convected derivative (see Appendix A) – for a particular value of the mobility parameter α. The figure makes it plain that bead formation is not seen in the case of these two models.

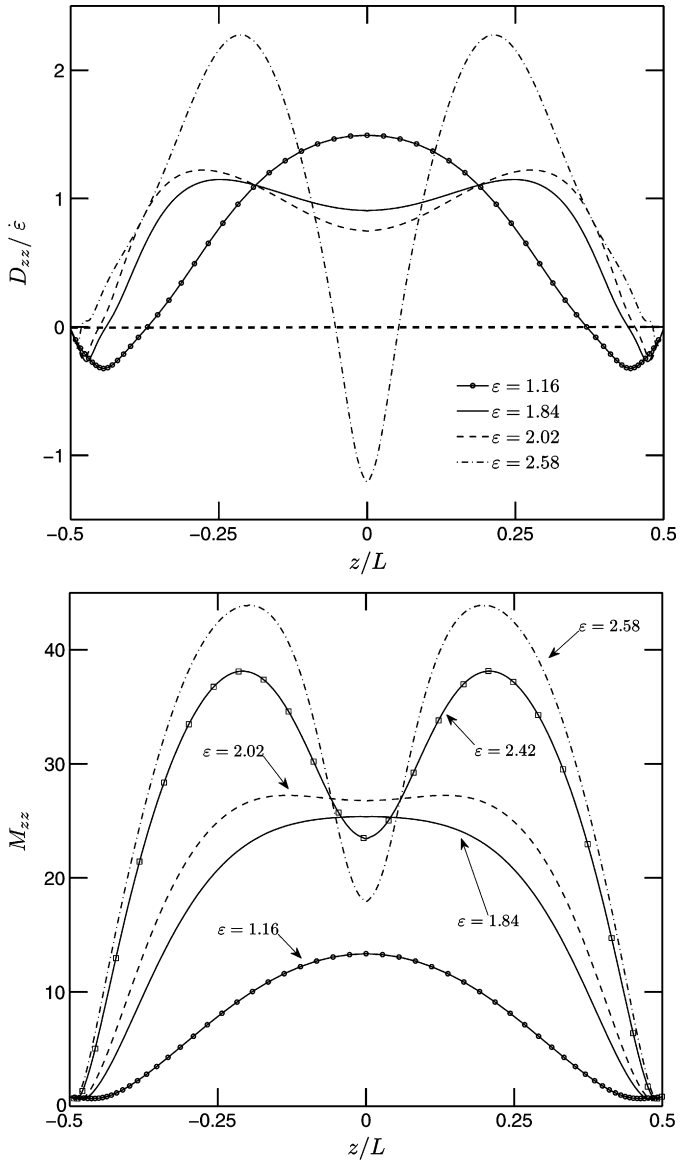

Fig. 5. Variation of the axial component of the rate-of-strain tensor D_{zz} normalized with $\dot{\varepsilon}$ (top) and that of the conformation tensor M_{zz} (bottom) along the free surface at different strains. Here, $\Lambda_0 = 0.334$, $Re = 0$, $Ca = 9.86$, $De = 1.89$, $\beta = 0.262$, $\xi = 0.26$, and $\epsilon = 0.035$.

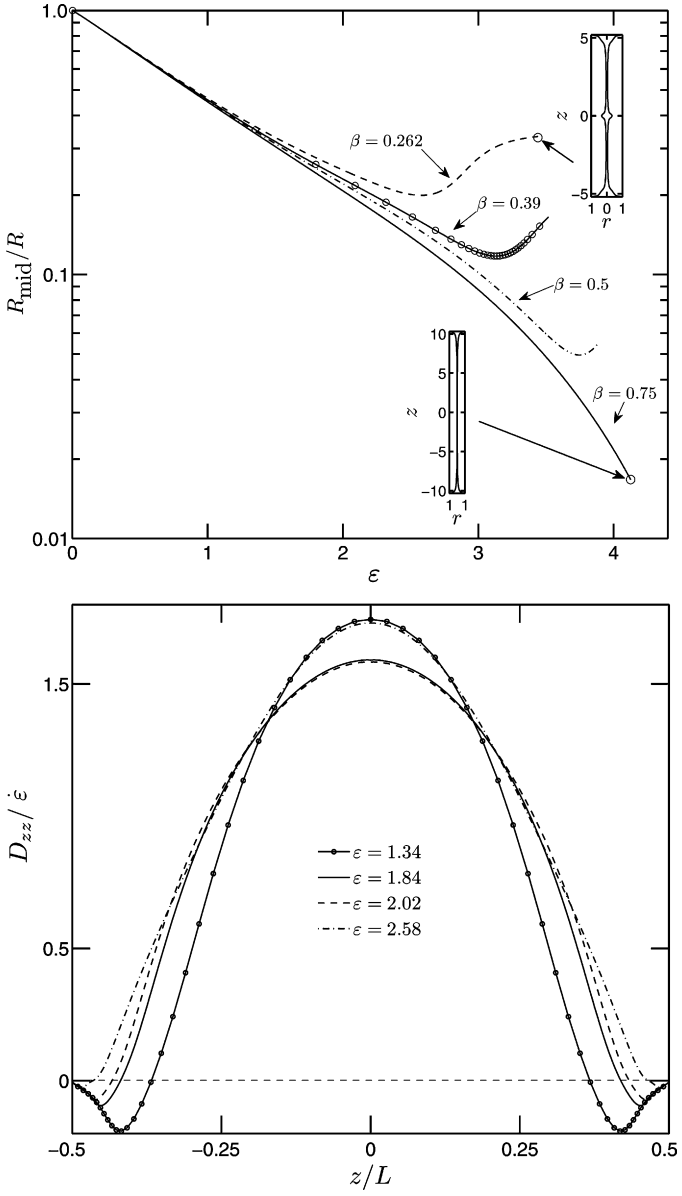

Fig. 6. Top: variation of the mid-filament radius R_{mid}/R with Hencky strain ε at different β. The insets show filament profiles at different strains for $\beta = 0.262$ and 0.75. Bottom: variation of the axial component of the rate-of-strain tensor D_{zz} normalized with $\dot{\varepsilon}$ along the free surface at $\beta = 0.75$ and different strains. Here, $\Lambda_0 = 0.334$, $Re = 0$, $Ca = 9.86$, $De = 1.89$, $\xi = 0.26$, and $\epsilon = 0.035$.

Matallah et al. [19] report the development of asymmetry in the computed values of the physical variables about the $z = 0$ plane. (See, e.g., Fig. 5 of [19].) This is counter-intuitive, because, in the calculations, both plates are being separated at the same speed and gravity is absent. In our computations, however, we do not see any asymmetry developing in the field variables about the $z = 0$ plane. Fig. 3 shows the variation of the height of the free surface, i.e., the local value of the bridge radius, h, normalized with the plate radius R along the length of the filament at the strain of 3.6. Although a bead can be seen at the center of the filament, the filament profile is symmetric about $z = 0$. The figure also shows the variation of the axial component of the rate-of-strain tensor, D_{zz}, and that of the conformation tensor, M_{zz}, along the axis of symmetry ($r = 0$) at the

strain of $\varepsilon = 3.6$. It can be seen that the profiles show two identical peaks resembling "double humps" but with no asymmetry about the $z = 0$ plane. The two maxima, one each in the two halves of the filament, have equal values. We do not see asymmetry at other radial locations as well (not shown).

The results shown earlier make it plain that a bead-like structure appears only in the presence of the GS convected derivative in the PTT equation ($\xi \neq 0$). The effect of changing ξ on bead formation is studied next. The evolution of the mid-filament radius R_{mid} with strain ε at $\xi = 0.13$ and 0.26 for $\Lambda_0 = 0.54$ and $Ca = 9.86$ is shown in Fig. 4. It can be seen that increasing ξ to 0.26 still results in the formation of a bead, but the onset of bead formation occurs early, at a lower strain, when compared to that in the case of $\xi = 0.13$. ξ is set as 0.26 and Ca as 9.86 in all the subsequent calculations presented in this paper.

The development of radial gradients in physical variables inside the filament is affected by its initial aspect ratio [43]. Filaments that are shorter initially give rise to more inhomogeneous profiles with regions of shear inside the filament. The effect of the initial aspect ratio, Λ_0, on the dynamics of bead formation is analyzed next. Fig. 4 also shows results for initial aspect ratios of 1 and 0.334. Filaments with smaller initial aspect ratios show earlier onset of bead formation. With an initial aspect ratio of 0.334, a bead forms at a strain of about 2.5. In all our subsequent analyses, we set $\Lambda_0 = 0.334$.

Fig. 5 shows the variation of the axial component of the rate-of-strain tensor, D_{zz}, along the free surface at strains of 1.16, 1.84, 2.02, and 2.58. The double hump feature appears at a strain of 1.84 and precedes the onset of bead formation which occurs around a strain of 2.5 (see Fig. 4). The double hump feature becomes more and more prominent at higher strains. The figure also shows the variation of the axial component of the conformation tensor, M_{zz}, along the free surface at different values of strain. A split in the maximum is also seen in the M_{zz} profiles but at a higher value of strain than that for D_{zz}. The double hump feature in the M_{zz} profile does not develop until a strain of 2.02, after the split in the maximum in the D_{zz} profile has already occurred. Thus, the split in the maximum of D_{zz} precedes the split in the maximum of M_{zz} and the formation of the bead.

The viscosity ratio, β, determines the coupling of the Cauchy momentum equation with the transport equation for the conformation tensor. The higher the value of β, the weaker is the coupling. As

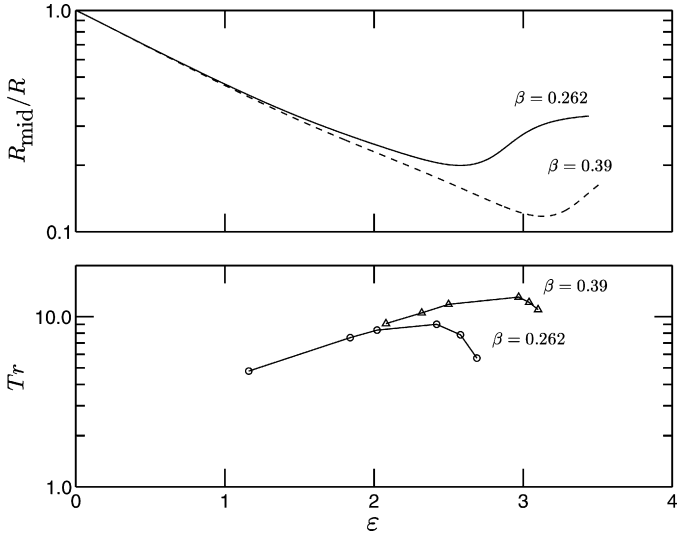

Fig. 7. Variation of the mid-filament radius R_{mid}/R and that of the transient Trouton ratio, Tr, with Hencky strain ε at $\beta = 0.262$ and 0.39. Here, $\Lambda_0 = 0.334$, $Re = 0$, $Ca = 9.86$, $De = 1.89$, $\xi = 0.26$, and $\epsilon = 0.035$.

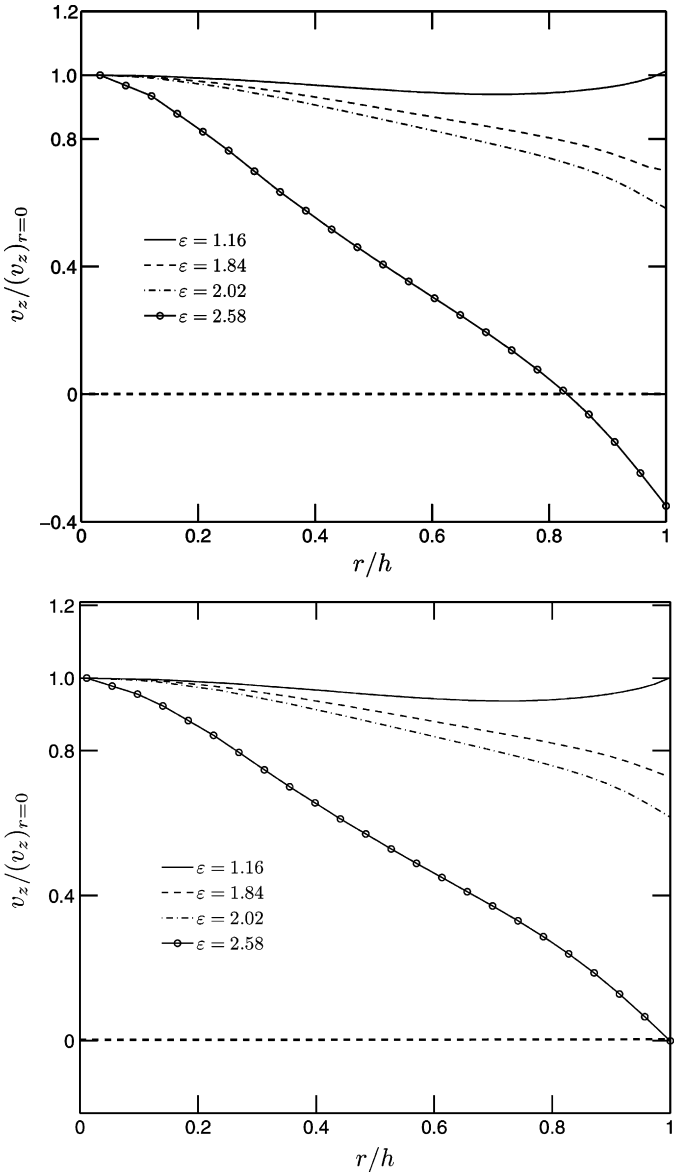

Fig. 8. Radial variation of the axial velocity v_z normalized with its value at the axis of symmetry ($r = 0$) for different strains at $z/L = 0.05$ (top) and $z/L = 0.1$ (bottom). h is the height of the free surface at these axial locations. Here, $\Lambda_0 = 0.334$, $Re = 0$, $Ca = 9.86$, $De = 1.89$, $\beta = 0.262$, $\epsilon = 0.035$, and $\xi = 0.26$.

demonstrated earlier, the split in the maximum of D_{zz} is followed by the formation of a bead. Because the computation of velocity (and hence **D**) is affected by the coupling of the momentum and the conformation transport equations, the effect of increasing β on the dynamics of PTT filaments is studied next. Fig. 6 shows the evolution of the mid-filament radius for $\beta = 0.262$, 0.39, 0.5, and 0.75. As with the case of varying ξ, varying β results in changing the onset of bead formation. As β increases and the coupling between the momentum and the conformation transport equation becomes weak, the onset of bead formation is delayed. For example, while bead formation starts around a strain of 2.5 when $\beta = 0.262$, a bead does not form until after a strain of 3.4 in the case of $\beta = 0.5$. No bead is observed to form for $\beta = 0.75$ at all strains until $\varepsilon = 4.13$, which is the limit of our calculations for this particular case. Fig. 6 also shows the variation of D_{zz} along the free surface for $\beta = 0.75$ at different strains. Clearly, the double hump feature seen in the case of $\beta = 0.262$ (see Fig. 5) is absent when $\beta = 0.75$.

The resistance to the thinning of filaments is quantified by the Trouton ratio $Tr = (T_{zz} - T_{rr})/\eta_0\dot{\varepsilon}$. In the case of PTT filaments with a non-zero ξ, the transient Trouton ratio shows a maximum around the strain value at which a bulge appears at the center of the filament. This can be seen in Fig. 7 which shows the variation of Tr with Hencky strain ε at $\beta = 0.262$ and 0.39. Here, Tr is computed using the Type IB formula of Yao et al. [44]. The maximum in Tr appears, however, after the split in the maximum of D_{zz} occurs. For example, when $\beta = 0.262$, the split in the maximum of D_{zz} occurs at a strain of 1.84 (see Fig. 5) whereas the maximum in Tr occurs at $\varepsilon > 2$. This suggests that the maximum in Tr is an effect of, rather than a cause for, the formation of the bulge at the center which disrupts the extensional flow inside the filament and thus lowers the Trouton ratio.

Fig. 8 shows the variation of the axial velocity, v_z, across axial cross-sections at $z/L = 0.1$ and 0.05 near the mid-filament region for strains of 1.16, 1.84, 2.02, and 2.58. Clearly, the axial velocity varies in the radial direction at these locations (i.e., $\partial v_z/\partial r \neq 0$). In other words, the flow at these locations has a shear component in it. In step and transient shear flows, equations with the GS convected derivative are known to exhibit oscillations in stress (for an illustration, see Appendix B). Fig. 9 shows the variation of the shear stress T_{rz}/G along the free surface at different strains for $\beta = 0.262$ and 0.75. The results are plotted for only one half of the filament ($0 \le z/L \le 0.5$); the results for the other half are the same in absolute value but have the opposite sign as the shear stress is an odd function of z/L. Whereas the shear stress when $\beta = 0.75$ increases monotonically with z/L until the end-effects are seen (due to the curved interface near the rigid plates) at all strains, it oscillates with strain (time) along the free surface when $\beta = 0.262$. (The inset in the figure shows details of the fluctuations in T_{rz}/G at $z/L = 0.1$ and $\beta = 0.262$ for different values of strain.) Thus, increasing β dampens the oscillations in the shear stress inside the filament. The resulting negative shear near the mid-filament at strain values greater than 2.5 when $\beta = 0.262$ drives the flow toward the center of the filament. The same phenomenon occurs in the other half of the filament; as a consequence, a bead starts forming at the center of the filament.

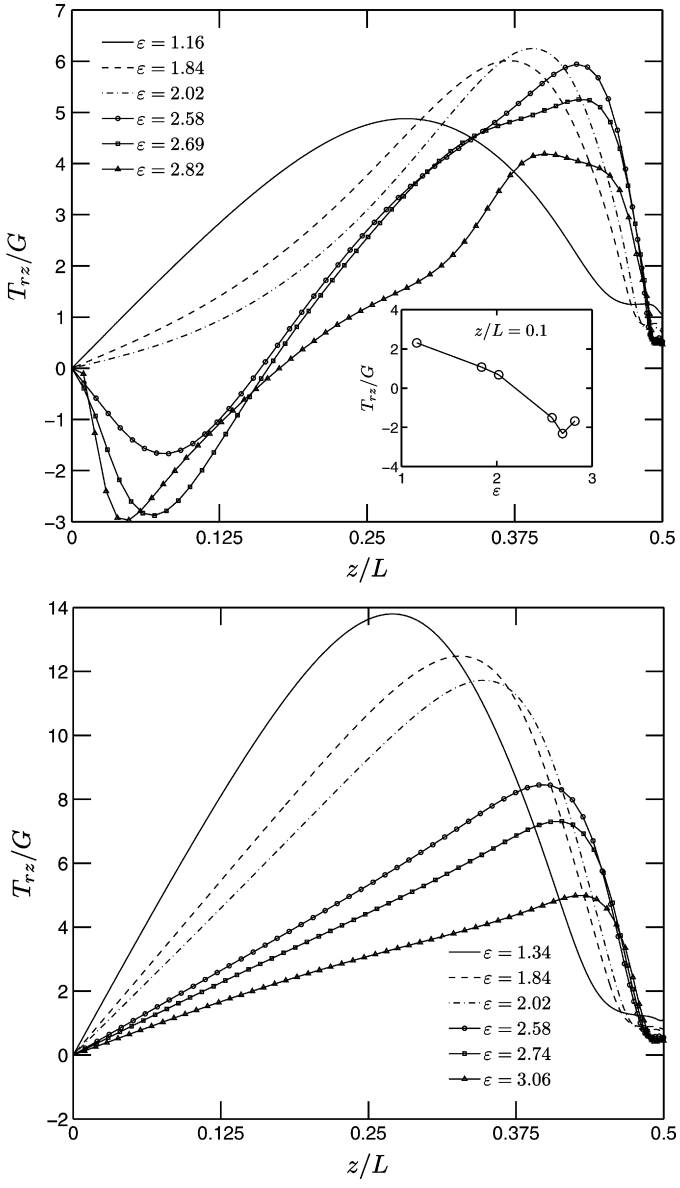

Fig. 9. Variation of the shear stress T_{rz}/G along the free surface in one half of the filament ($0 \le z/L \le 0.5$) for $\beta = 0.262$ (top) and $\beta = 0.75$ (bottom) at different strains. The inset in the top figure shows the variation of the shear stress with strain ε at $z/L = 0.1$. Here, $\Lambda_0 = 0.334$, $Re = 0$, $Ca = 9.86$, $De = 1.89$, $\epsilon = 0.035$, and $\xi = 0.26$.

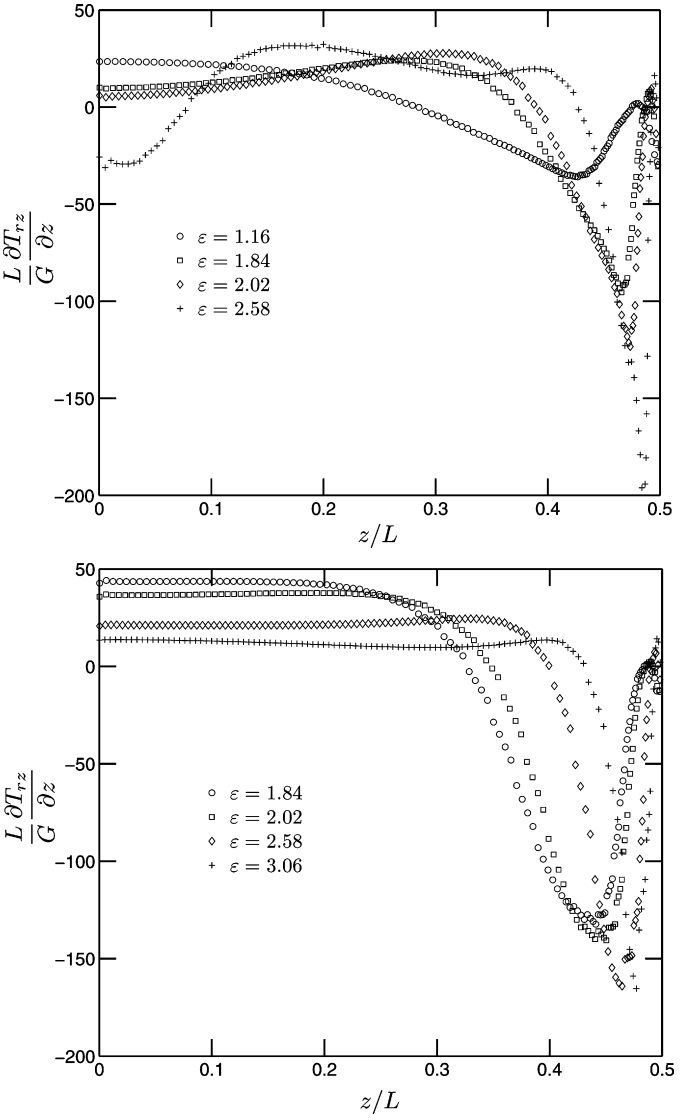

Fig. 10. Variation of the derivative of the shear stress T_{rz}/G with respect to z/L along the free surface in one half of the filament ($0 \le z/L \le 0.5$) for $\beta = 0.262$ (top) and $\beta = 0.75$ (bottom) at different strains. Here, $\Lambda_0 = 0.334$, $Re = 0$, $Ca = 9.86$, $De = 1.89$, $\epsilon = 0.035$, and $\xi = 0.26$.

Fig. 10 shows the variation of the derivative of the shear stress with respect to the axial position, $(L/G)\,\partial T_{rz}/\partial z$, along the free surface at different strains. The derivative is calculated from the data in Fig. 9 using centered differences. At small strains, for $\beta = 0.262$, this derived quantity is constant near the center of the filament and then decreases along the length of the free surface until end-effects become important. At strains greater than or equal to 1.84 – the strain at which the split in the maximum of D_{zz} is first seen (see Fig. 5) – this derived quantity *increases* first with z/L before the end-effects are seen. Thus, the occurrence of the split in the maximum of D_{zz} coincides with the change in the slope of the $(L/G)\,\partial T_{rz}/\partial z$ vs. z/L curve. When β is increased to 0.75, $(L/G)\,\partial T_{rz}/\partial z$ remains constant in the mid-filament region for all values of strain computed. As a consequence, the location of the maximum in D_{zz} does not migrate from the center of the filament (see the bottom plot in Fig. 6) and no bead forms. It is to be noted that at the limit of our computations ($\varepsilon = 4.13$), we do not see when $\beta = 0.75$ any indication of bead formation either: that is, we do not observe the slope of $(L/G)\,\partial T_{rz}/\partial z$ changing in the mid-filament region or a split in the maximum of D_{zz}.

The unusual behavior of the PTT model in step shear could also explain the difference between the present calculations and that of Matallah et al. [19] as they use a different numerical method in their computations. By contrast, when $\xi = 0$, the flow inside the filament is nearly plug-flow, i.e., $\partial v_z/\partial r = 0$ (not shown).

4. Concluding remarks

The breakup of viscoelastic filaments in filament stretching experiments is preceded by the formation of the beads-on-string morphology in some cases. Computationally, such an event was not reproduced with strain-hardening models until recently [19]. Bead-like structures on filaments were reported in calculations with the PTT model that has the Gordon–Schowalter (GS) convected derivative. This starkly different behavior of the PTT model with the GS convected derivative has been further examined in this paper.

The occurrence of a bead is found to be preceded first by the split in the maximum of the axial component of the rate-of-strain tensor inside the filament and next by a similar split in the maximum of the axial elastic stress. Regions of shear form inside the filament during initial elongation due to the presence of a curved interface. This change happens quickly. As a consequence, the shear stress developed shows temporal oscillations, which is expected of a constitutive equation with the GS convected derivative [28]. The resulting shear stress in the mid-filament region, equal but with opposite signs in the two halves of the filament, drives the flow toward the center of the filament causing the formation of a bead there. Such oscillations in stress are dampened when β is increased and absent when ξ is set equal to zero.

Although we report bead formation in PTT filaments as has been done earlier by Matallah et al. [19], we see no asymmetry developing in physical variables about the $z = 0$ plane as claimed in [19]. This finding accords with the symmetric conditions imposed on the problem. Further, the occurrence of the bead is attributed here to the presence of GS convected derivative in the PTT equation unlike [19] where it is said to be an effect of strain-hardening. A different numerical scheme is adopted in [19] which gives qualitatively the same (formation of a bead) but quantitatively different (disagreements in Fig. 2) results from our calculations. This observation highlights the need for a further investigation into the stability of the dynamical system that consists of the PTT equation with a non-zero ξ.

Acknowledgments

This work was supported by the National Science Foundation/Engineering Research Center (NSF/ERC) at Rutgers, Purdue, NJIT, and UPRM on Structured Organic Particulate Systems (SOPS). MP thanks NSF for grants CTS-CAREER-0134389 and CTS-ITR-0312764.

Appendix A. The Giesekus constitutive equation

The transport equation for the conformation tensor in the Giesekus model [20] is

$$\frac{\partial \mathbf{M}}{\partial t} = -\mathbf{v}\cdot\nabla\mathbf{M} + \zeta(\mathbf{M}\cdot\mathbf{D} + \mathbf{D}\cdot\mathbf{M}) + \mathbf{M}\cdot\mathbf{W} + \mathbf{W}^T\cdot\mathbf{M} - \frac{1}{\lambda}[(\alpha-1)\mathbf{I} + (1-2\alpha)\mathbf{M} + \alpha\mathbf{M}^2] \quad (A.1)$$

where $\zeta = 1$ and α is a model parameter (called the mobility parameter). The elastic stress $\boldsymbol{\sigma}$ is obtained from the conformation tensor $\mathbf{M}$ as $\boldsymbol{\sigma} = G(\mathbf{M} - \mathbf{I})$.

Appendix B. Response of the PTT constitutive equation to step shear

Equations with the GS convected derivative are known to show unphysical oscillations in stress when a step change is applied to the strain rate in transient shear flows [28]. Fig. B.1 shows this behavior in the case of the PTT equation for $\xi = 0.26$. The shear stress, σ_{xy}/G, is computed by solving Eq. (2) for transient shear flows. The dimensionless shear rate $\lambda\dot{\gamma}$ is instantaneously changed from one value to another. The computations are started with the steady shear value that corresponds to the strain-rate at time $t/\lambda = 0$. Fig. B.1 also shows the stress behavior for the affine case ($\xi = 0$). While the stress oscillates before reaching a steady value when $\xi \neq 0$, it reaches the same with an overshoot and no oscillations in the affine case (which is expected of a viscoelastic liquid and hence physical). Note that the steady shear value for $\xi = 0$ is higher than that for $\xi = 0.26$. This is because the PTT model shows increased shear thinning as ξ increases.

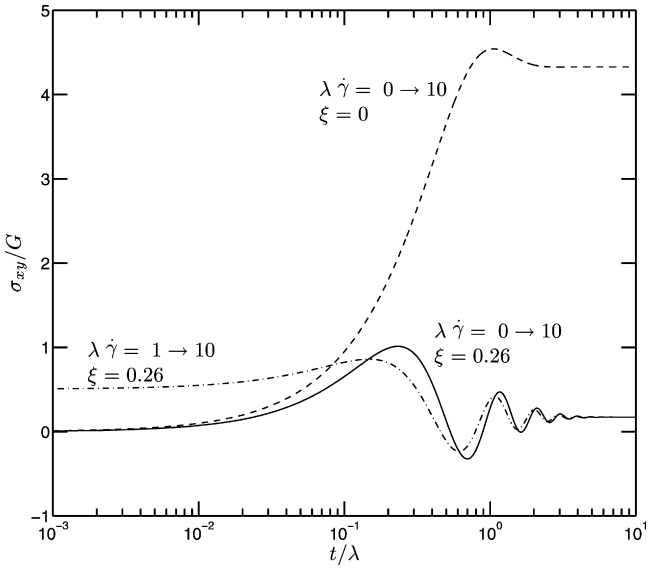

Fig. B.1. Development of the shear stress σ_{xy}/G with time t/λ when the dimensionless shear rate $\lambda\dot{\gamma}$ is subjected to step changes in the PTT model with ($\xi = 0.26$) and without ($\xi = 0$) the GS convected derivative. Here $\epsilon = 0.035$.

References

[1] O.A. Basaran, Small-scale free surface flows with breakup: drop formation and emerging applications, AIChE J. 48 (2002) 1842–1848.
[2] G.Y. Park, G.M. Harrison, Effects of elasticity on the spraying of a non-Newtonian fluid, Atom. Sprays 18 (2008) 243–271.
[3] C.H. Park, H.J. Jeong, J.J. Jung, G.Y. Lee, S.C. Kim, T.S. Kim, S.H. Yang, H.C. Chung, S.Y. Rha, Fabrication of high quality cDNA microarray using a small amount of cDNA, Int. J. Mol. Med. 13 (2004) 675–679.
[4] P. Calvert, Printing cells, Science 318 (2007) 208–209.
[5] Y. Amarouchene, D. Bonn, J. Meunier, H. Kellay, Inhibition of the finite-time singularity during droplet fission of a polymeric fluid, Phys. Rev. Lett. 86 (2001) 3558–3561.
[6] M. Goldin, H. Yerushalmi, R. Pfeffer, R. Shinnar, Breakup of a laminar capillary jet of a viscoelastic fluid, J. Fluid Mech. 38 (1969) 689–711.
[7] P.T. McGough, O.A. Basaran, Repeated formation of fluid threads in breakup of a surfactant-covered jet, Phys. Rev. Lett. 96 (2006) 054502.
[8] J.E. Matta, R.P. Tytus, Liquid stretching using a falling cylinder, J. Non-Newtonian Fluid Mech. 35 (1990) 215–229.
[9] T. Sridhar, V. Tirtaatmadja, D.A. Nguyen, R.K. Gupta, Measurement of extensional viscosity of polymer solutions, J. Non-Newtonian Fluid Mech. 40 (1991) 271–280.
[10] X. Zhang, R.S. Padgett, O.A. Basaran, Nonlinear deformation and breakup of stretching liquid bridges, J. Fluid Mech. 329 (1996) 207–245.
[11] P.P. Bhat, O.A. Basaran, M. Pasquali, Dynamics of viscoelastic filaments: low capillary number flows, J. Non-Newtonian Fluid Mech. 150 (2008) 211–225.
[12] Y.-C. Liao, E.I. Franses, O.A. Basaran, Deformation and breakup of a stretching liquid bridge covered with an insoluble surfactant monolayer, Phys. Fluids 18 (2006) 022101.
[13] R. Suryo, O.A. Basaran, Local dynamics during pinch-off of liquid threads of power law fluids: scaling analysis and self-similarity, J. Non-Newtonian Fluid Mech. 138 (2006) 134–160.
[14] K. Foteinopoulou, V.G. Mavrantzas, J. Tsamopoulos, Numerical simulation of bubble growth in Newtonian and viscoelastic filaments undergoing stretching, J. Non-Newtonian Fluid Mech. 122 (2004) 177–200.
[15] K. Foteinopoulou, V.G. Mavrantzas, Y. Dimakopoulos, J. Tsamopoulos, Numerical simulation of multiple bubbles growing in a Newtonian liquid filament undergoing stretching, Phys. Fluids 18 (2006) 042106.
[16] M.S.N. Oliveira, G.H. McKinley, Iterated stretching and multiple breads-on-a-string phenomena in dilute solutions of highly extensible flexible polymers, Phys. Fluids 17 (2005) 071704.
[17] R. Sizaire, V. Legat, Finite element simulation of a filament stretching extensional rheometer, J. Non-Newtonian Fluid Mech. 71 (1997) 89–107.
[18] M. Yao, S.H. Spiegelberg, G.H. McKinley, Dynamics of weakly strain-hardening fluids in filament stretching devices, J. Non-Newtonian Fluid Mech. 89 (2000) 1–43.
[19] H. Matallah, M.J. Banaai, K.S. Sujatha, M.F. Webster, Modelling filament stretching flows with strain-hardening models and sub-cell approximations, J. Non-Newtonian Fluid Mech. 134 (2006) 77–104.
[20] H. Giesekus, A simple constitutive equation for polymer fluids based on the concept of deformation-dependent tensorial mobility, J. Non-Newtonian Fluid Mech. 11 (1982) 69–109.
[21] R.A. Bird, C.F. Curtiss, R.C. Armstrong, O. Hassager, Dynamics of Polymeric Liquids, vol. 2, 2nd edition, John Wiley & Sons, New York, 1987.
[22] M.D. Chilcott, J.M. Rallison, Creeping flow of dilute polymer solutions past cylinders and spheres, J. Non-Newtonian Fluid Mech. 29 (1988) 381–432.
[23] N. Phan-Thien, R.I. Tanner, A new constitutive equation derived from network theory, J. Non-Newtonian Fluid Mech. 2 (1977) 353–365.
[24] R.J. Gordon, W.R. Schowalter, Anisotropic fluid theory: a different approach to the dumbbell theory of dilute polymer solutions, Trans. Soc. Rheol. 16 (1972) 79–97.
[25] H. Matallah, K.S. Sujatha, M.J. Banaai, M.F. Webster, Single and multi-mode modelling for filament stretching flows, J. Non-Newtonian Fluid Mech. 146 (2007) 92–113.
[26] M.D. Johnson, D. Segalman, A model for viscoelastic fluid behavior which allows non-affine deformation, J. Non-Newtonian Fluid Mech. 2 (1977) 225–270.
[27] A.S. Lodge, J. Meissner, On the use of instantaneous strains, superposed on shear and elongational flows of polymeric liquids, to test the Gaussian network hypothesis and to estimate the segment concentration and its variation during flow, Rheol. Acta 11 (1972) 351–352.
[28] R.G. Larson, Constitutive Equations for Polymer Melts and Solutions, 1st edition, Butterworths, Boston, 1988.
[29] M. Pasquali, L.E. Scriven, Free surface flows of polymer solutions with models based on conformation tensor, J. Non-Newtonian Fluid Mech. 108 (2002) 363–409.
[30] M. Pasquali, L.E. Scriven, Theoretical modeling of microstructured liquids: a simple thermodynamic approach, J. Non-Newtonian Fluid Mech. 120 (2004) 101–135.
[31] M. Grmela, P.J. Carreau, Conformation tensor rheological models, J. Non-Newtonian Fluid Mech. 23 (1987) 271–294.
[32] A.N. Beris, B.J. Edwards, Thermodynamics of Flowing Systems with Internal Microstructure, 1st edition, Oxford University Press, Oxford, 1994.
[33] R.J.J. Jongschaap, K.H. de Haas, C.A.J. Damen, A generic matrix representation of configuration tensor rheological models, J. Rheol. 38 (1994) 769–796.
[34] N. Phan-Thien, A nonlinear network viscoelastic model, J. Rheol. 22 (1978) 259–283.
[35] M. Pasquali, Polymer Molecules in Free Surface Coating Flows, PhD Thesis, University of Minnesota, Minneapolis, MN, 2000. Available from UMI, Ann Arbor, MI, order number 9963019.
[36] J.M. de Santos, Two-phase Cocurrent Downflow through Constricted Passages, PhD Thesis, University of Minnesota, Minneapolis, MN, 1991. Available from UMI, Ann Arbor, MI, order number 9119386.
[37] M.J. Szady, T.R. Salamon, A.W. Liu, R.C. Armstrong, R.A. Brown, A new mixed finite element method for viscoelastic flows governed by differential constitutive equations, J. Non-Newtonian Fluid Mech. 59 (1995) 215–243.
[38] R. Guénette, M. Fortin, A new finite element method for computing viscoelastic flows, J. Non-Newtonian Fluid Mech. 60 (1995) 27–52.
[39] P.M. Gresho, R.R. Lee, R.C. Sani, On the time-dependent solution of the incompressible Navier–Stokes equations in two and three dimensions, in: C. Taylor, K. Morgan (Eds.), in: Recent Advances in Numerical Methods in Fluids, vol. 1, Pineridge Press, Swansea, UK, 1980, p. 27.
[40] I.S. Duff, A.M. Erisman, J.K. Reid, Direct Methods for Sparse Matrices, 1st edition, Oxford University Press, Oxford, 1989.
[41] L.E. Scriven, Dynamics of a fluid interface – equation of motion for Newtonian surface fluids, Chem. Eng. Sci. 12 (1960) 98–108.
[42] R. Aris, Vectors, Tensors, and the Basic Equations of Fluid Mechanics, Prentice-Hall, Englewood Cliffs, NJ, 1962.
[43] M. Yao, G.H. McKinley, Numerical simulation of extensional deformations of viscoelastic liquid bridges in filament stretching devices, J. Non-Newtonian Fluid Mech. 74 (1998) 47–88.
[44] M. Yao, G.H. McKinley, B. Debbaut, Extensional deformation, stress relaxation and necking failure of viscoelastic filaments, J. Non-Newtonian Fluid Mech. 79 (1998) 469–501.